EFFECT OF SIDEPINS ON THE THERMOHYDRAULIC CHARACTERISTICS OF AN ARRAY OF INTERNAL PIN FINS

S.M. Roux, G.I. Mahmood, & J.P. Meyer*

Department of Mechanical and Aeronautical Engineering, University of Pretoria, Gauteng, RSA

*Address all correspondence to: G.I. Mahmood, Department of Mechanical and Aeronautical Engineering, University of Pretoria, Gauteng, RSA, E-mail: gazi.mahmood@up.ac.za

Original Manuscript Submitted: mm/dd/yyyy; Final Draft Received: mm/dd/yyyy

Few of the investigations on the thermohydraulic performance of the arrays of short pin fins in channels have addressed and quantified the impact of the pins located on the sidewalls. In the confined space of a channel, the pins on the sidewalls are placed sometimes to justify the flow periodicity and flow-area uniformity in the channel with multiple pin rows. The present investigation measures the influences of the sidewall pins on the flow field in a pin-fin channel employing arrays of circular pin fins in 13 staggered rows. The flow measurements are also obtained in the same pin-fin channel without the presence of the sidewall pins for comparisons. Reynolds number (Re) based on the channel hydraulic diameter and mean flow velocity for the measurements varies between 5000 and 50,000. The pin-fin array employs a spacing of two pin diameters between the pins in the streamwise and transverse directions. The results of pressure distributions, pressure losses, heat transfer coefficients, and flow temperature distributions along the pin-fin rows indicate that the sidewall pins have little influence generally on the local secondary flow structures. The differences in the measured data are primarily caused by the redistributions of local mass flux and flow acceleration as the pins on the sidewalls are employed. Because of the extra flow blockage imposed by the sidewall pins in the sidewall gap, the friction factor is 15–30% higher and the overall total pressure loss coefficient is 1–6% higher over the Reynolds number range with the sidewall pins than without the sidewall pins. The average Nusselt on the endwall differs by less than 4% between the cases of sidewall pins and no sidewalls pins irrespective of the Reynolds numbers tested.

KEY WORDS: *array, pin fin, augmentation, five-hole probe*

1. INTRODUCTION

Flow and heat transfer investigations in channels with arrays of short pin fins have been active in the last few decades. The pin fins provide structural integrity to the channel walls in addition to improving the convective heat transfer at the channel endwalls. Past studies have investigated the pin geometry (Chang et al., 2008; Huang et al., 2016; Tanda, 2001), pin spacing (Axtmann et al., 2016; Lawson et al., 2011), and surface augmentation (Pretorius et al., 2017; Rao et al., 2012) in the rectangular channel to optimize the heat transfer augmentation relative to the pressure penalty. Research has also been done on microscale pin-fin channels (Xu and Wu, 2018).

In the confined space of a channel, pins are sometimes placed on the sidewall to maintain the flow periodicity and flow-area uniformity. However, the effects of the sidepins in the channel on the local flow, temperature fields, and endwall heat transfer are not investigated in detail. It is the local secondary flows that are primarily responsible for the heat transfer enhancement in the pin-fin channel. The present experimental study investigates the local flows, air temperatures, and endwall heat transfer in a pin-fin channel with pins located on the sidewall.

The reviews by Armstrong and Winstanley (1988) on the investigations in pin-fin channels include the effects of pin spacing and pin height of the pin-fin array on the heat transfer. The correlations of Metzger et al. (1982) predict pressure losses and endwall heat transfer coefficients for a range of pin spacings in the pin-fin array. The study by

NOMENCLATURE

A_{ch}, A_s	unobstructed cross section of channel and exposed heated surface area, respectively	p_o, p_x	surface pressure at reference and along surface, respectively
a, b, c, d	parameters in friction factor correlations	$p_{t,o}$, $p_{t,x}$	total pressure at reference and channel section, respectively
C_p, $C_{p,e}$, $C_{p,t}$, $C_{p,w}$, $C_{pe,av}$, $C_{pt,av}$	pressure coefficients	Q_c	convection power at heated endwall
c_p	specific heat of air	R1, R2, ..., R13	streamwise pin-row number
D, D_h	pin diameter and channel hydraulic diameter, respectively	T, T^*	local and normalized air temperature, respectively
f, f_o, f_{o1}	friction factors	T_o	reference temperature of air
H	pin height	$T_{w,x}$, $T_{m,x}$	local endwall and bulk-mean temperature, respectively
k_a	thermal conductivity of air	U	mass-averaged mean flow velocity
L	test section length	u^*	streamwise local velocity ratio, u/U
M_a	mass flow rate of air through the channel, ($\rho_o U A_{ch}$)	W	test section width
Nu, Nu_0	endwall Nusselt number for pin-fin array and smooth channel, respectively	x, y, z	local coordinates: streamwise, transverse, and vertical lengths, respectively
Nu_{av}	area-averaged Nusselt number	**Greek Symbols**	
Nu^*, Nu^*_{av}	Nusselt number ratio ($\mathrm{Nu}/\mathrm{Nu}_0$, $\mathrm{Nu}_{av}/\mathrm{Nu}_0$)	μ	dynamic viscosity of air
		ρ	air density

Won et al. (2004) provides the role of the transverse secondary flows in the pin-fin array to enhance the local heat transfer at the endwall.

The influences of different pin geometries on the pressure drop and heat transfer in the pin-fin array are studied and compared with the results of the circular pins by Goldstein et al. (1994), Chyu et al. (1998), Li et al. (1998), Tanda (2001), Chang et al. (2008), and Huang et al. (2016). The investigations of Chang et al. (2008) in a detached circular pin-fin array produce significant reduction in the pressure losses with only a moderate heat transfer penalty relative to the attached pins. Chang et al. (2008) attribute the higher thermal performance in the detached pin array than those in the attached pin array to the greater freestream area (less blockage). The lateral freestream area between the sidewall and pin-fin array also provides less blockage and pressure losses compared to the pin-fin array with the sidepins. However, the effects on the local flow field with the sidepins relative to those without them cannot be expected to be similar to those of Chang et al. (2008). This is because the flow blockage configuration in the pin-fin array is different with the sidepins present. Ames et al. (2005) investigated the friction factor and augmentation of heat transfer in a pin-fin array with circular pin fins on the channel sidewall. The effects of the sidepins on the results are not specifically identified.

While the recent pin-fin channel investigations provide plethora of data in the thermohydraulically developed region of the pin array, very little information in the developing region of flow along the pin-fin array are available. The data in the flow developing region is important for the applications where the space constraints require short length of channels where only few rows of pin fins can be employed, e.g., cooling channels in electronic chips, combustor liners, and bearing housings. The objectives of the present investigation are to quantify the thermohydraulic effects of the sidewall pins in both the developing and developed regions of flow in the pin-fin channel with particular emphasis

on the developing region. The experiments measure the local flow field and endwall heat transfer along a thirteen-row staggered pin-fin array in a rectangular channel with and without the sidepins. The circular pin geometry is employed in the array while the one-half circle pin geometry is used as the sidepins to maintain the flow symmetry and periodicity of the pin-fin array. The results include the distributions of the wall-static pressure, friction factors, total pressure loss, endwall heat transfer coefficient, and air temperature for different Reynolds numbers. The data are then compared between the cases with and without sidepins to show the influences of the sidepins. The results are important to optimize the thermal performance of the pin-fin channels.

2. EXPERIMENTAL FACILITY AND METHODS

2.1 Wind Tunnel

The experimental facility shown schematically in Fig. 1(a) is a low-speed wind tunnel which operates under the suction of two axial fans with a total power of 11 kW. The laboratory air first enters the wind tunnel through a honeycomb screen followed by a two-dimensional contraction section of ratio 4:1. It then passes through a rectangular channel of cross section same as that of the test section. The channel length of ten hydraulic diameters causes the air flow to be fully developed hydrodynamically before entering the test section. Following the test section in Fig. 1(a), a rectangular-to-round transition section and a metered pipe section with an ISO 5167-1 standard orifice plate are employed. The two axial fans, one of which is connected to a speed controller, are located on the downstream end of the metered pipe section. The Reynolds number in the test channel is controlled by either adjusting the fan speed or running one fan only. The walls of the wind tunnel are made of acrylic plastic. The pressure difference across the orifice estimates the mass flow rate and mass-averaged velocity in the tunnel.

2.2 Test Section

The test section having a streamwise length of 1.85 m shown in Fig. 1(b) employs a flow cross section of aspect ratio 7.81:1 with a width of 50 cm. The cylindrical pins of diameter 50 mm and height 64 mm ($H/D = 1.28$) are arranged

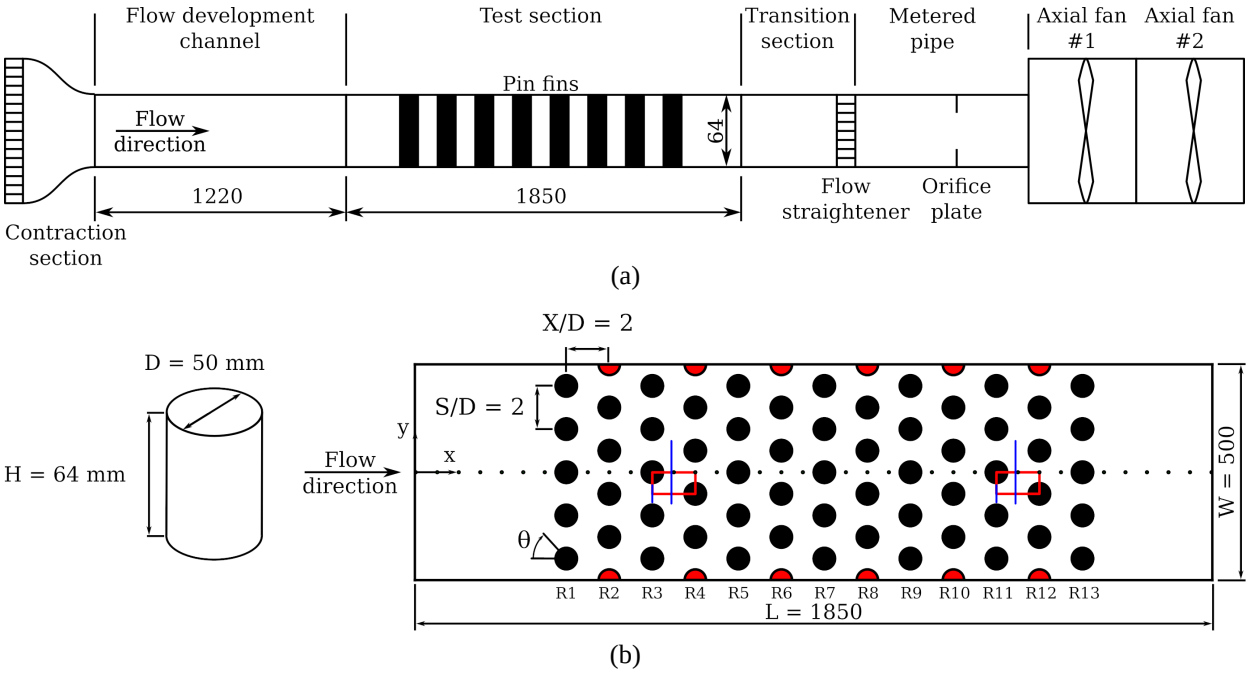

FIG. 1: Schematic of the (a) experimental facility and (b) test section and pin-fin geometry (dimensions are in mm)

in thirteen staggered rows streamwise. The dark circles in Fig. 1(b) represent the locations of the pin fins on the test section endwall. The pin rows are staggered with 5 pins and 4 pins of full diameter alternating with both a streamwise and transverse spacing (X/D, S/D) of 2.0. The pins are secured in place with screws on the two endwalls. The streamwise row numbers of the pin (pin row 1, pin row 2, pin row 3, ...) are indicated by R1, R2, R3, ... in Fig. 1(b). Commercial grade cylindrical rods of acrylic plastic are used to construct the pins. The red half-circles in Fig. 1(b) show the locations of the sidewall pins on the endwall. The half-circle pins are exactly one-half of the full diameter pins and flushed against the sidewalls with screws from the endwalls. The spacing, S/D, between the sidewall pin and the adjacent pin in the same row is also 2.0. Accounting the two one-half pins in each even-numbered row the pin-fin array then employs 5 full pins and the same flow cross section at each pin-fin row when the sidepins are employed.

Static pressure tap holes of diameter 1 mm with a spacing of 50 mm are drilled along the streamwise direction in one of the endwalls. As shown in Fig. 1(b), the endwall pressure taps indicated by the black dots are located in the middle or 250 mm from the sidewalls. To obtain detailed pressure distributions on the endwall, arrays of pressure taps in both the streamwise and transverse (x, y) directions are drilled in the regions marked by the small rectangular areas in Fig. 1(b) between R3 and R4 and between R11 and R12. Figure 1(b) also indicates the locations of four cut-out slots by blue lines along the transverse pitch (y direction) in the endwall between R3 and R4 and between R11 and R12. Two of the slots are located along the pin-row centerline in R3 and R11, and the other two are located $0.9D$ downstream of R3 and R11. The slot spans D and $2D$ along the row-centerline and downstream of the pin row, respectively, in the top endwall. A five-hole pressure probe and a temperature probe are traversed through the slots to measure the flow field in the transverse normal planes at the slot locations.

2.3 Surface Pressure and Flow Field Measurements

The wall static pressure taps are connected to a differential pressure transducer through plastic tubings and an electro-mechanical scanner. The scanner is comprised of two mating discs with one disc connected to all the pressure taps and the second disc connected to the pressure transducer. An electric impulse input of voltage activates a stepper motor to rotate the scanner disc on the transducer side by a certain angle about its axis. Each rotation of the disc then connects one pressure tap to the transducer at a time. The voltage output signal from the pressure transducer is digitized and recorded using an Agilent™ 34970 data acquisition system at a sampling rate of 2 Hz for 25 s at each pressure tap. The time-averaged voltage output from each pressure tap is then converted to a pressure value by applying the appropriate calibration curve.

The five-hole total pressure probe that obtains the flow field data has a tip diameter of 1.6 mm. The probe scans the y transverse plane using a two-axis motorized traverse at a spatial resolution of 2.5 mm × 2.5 mm. The pressure signals from the five-hole probe are converted to voltages through five differential pressure transducers and then recorded through the Agilent™ 34970 data acquisition system. The signals are time averaged from the sampling rate of 2 Hz for 25 s at each location. The signals are then converted to pressure values by applying the transducer calibrations, and then further to the static pressure, total pressure, and velocity vectors by applying the probe calibration curves, spatial corrections, and downwash velocity corrections as described by Ligrani et al. (1989a,b) and Paul et al. (2011). One single in-house Labview™ program is employed for the data acquisition and controlling of traverse motion to synchronize the probe travel and data acquisition.

The temperature probe employs a calibrated T-type thermocouple at the end of a pair of needle prongs mounted on one end of a rod holder. The probe scans the y transverse plane at a spatial resolution of 5 mm × 5 mm on the same traverse as used by the five-hole pressure probe. The probe motion-control and temperature data recorded through the Agilent™ 34970 system are also obtained using a single LabviewTM program. The temperature data at each location of the scan are time averaged over 25 s at 1 Hz.

2.4 Endwall Temperature Measurements

Heat transfer measurements are performed by heating both the endwalls of the test section with temperature measurements taken using thermocouples and thermal imaging at the bottom endwall. Convective heat flux into the flow is supplied by 1.6-mm-thick NEMA FR4 PCBs which are etched with a 35-μm-thick and 10-mm-wide continuous

copper channel. To maintain continuity in the heater circuit, the heater plates continue under the pin bases. A new set of endwalls with embedded thermocouples is used to replace the pressure-tapped endwalls. The PCB heater plates are attached to the endwalls on the flow side of the channel. The tips of the embedded thermocouples in the endwalls are in contact with the PCB-plate surface when they are assembled. The thermocouple tips are placed at the same locations as the pressure tap locations. Because of the symmetric boundary conditions about the channel mid-height, thermocouples are only placed in the bottom endwall. The pin fins are screwed in place using the screw holes in the heater plates and endwalls. The spacing between two endwalls is adjusted to make heater plates flush with the other endwalls of the wind tunnel. The heaters are connected in series to a 220 V 50 Hz AC power supply through an adjustable solid-state relay. The calibrated ammeter and voltmeter are used to monitor the supplied power. No heater is placed on the two sidewalls of the test channel. The test section is insulated with two layers of foam insulation of thermal conductivity 0.2 W/m·K to minimize heat losses. Thermocouples are placed across the first layer of insulation at different locations along the test section. Measuring the temperature differences across the insulation layer, the one-dimensional Fourier conduction law is applied to estimate the conduction heat losses through the insulation layers. Because of the placement of the heaters on the flow side of the endwalls, most of the heater power enters the air flow. The estimated conduction loss from each heater is under 5% of the total heater power. The measured current and voltage applied across each heater provide the total heat input power.

Thermal images of the bottom endwall are obtained using a A35 f9mm FLIR™ infra-red (IR) camera between the 11^{th} and 12^{th} pin-fin rows as indicated in the red rectangle region shown in Fig. 1(b). A cut-out section on the top endwall covered by a Zn–Se window allows the IR camera view on the target region. Fifteen calibrated thermocouples are embedded inside the bottom endwall at particular locations in contact with the heater plate and within the image area. The calibrated outputs from all the thermocouples are time averaged at 1 Hz over 25 s through the Agilent™ system. The thermocouple data and video streaming from the IR camera are recorded simultaneously and used to calibrate the thermal images employing the *in situ* technique illustrated by Sargant et al. (1998). As the Zn–Se window section has to be unheated during the IR imaging, thermocouple measurements at the endwall are also obtained at corresponding Re with a heated window section replacing the Zn–Se window. The temperatures at the corresponding thermocouple locations with and without the heated window section differ negligibly ensuring negligible effects of the unheated window on the IR image area. The video streaming from the IR camera is obtained at a frame rate of 60 Hz. A time-averaged image over a 30 s period is used for the image calibration. The image resolution of the camera is 320 × 256 pixels with 14 bit resolution providing a pixel size of 0.313 mm in the calibrated image of the endwall.

The convective power into the flow is obtained after subtracting the conduction losses through the endwall from the total electric power into the heater plates. The maximum endwall temperature of 80°C validates the assumptions of negligible effects of the buoyancy and radiation losses.

3. UNCERTAINTY ESTIMATES

Pressure transducers employed in the measurements are calibrated with a Setra Micro Calibrator™ Model 869 having an accuracy of 0.05 Pa and thermocouples are calibrated in a thermal bath against a PT100 temperature probe with an accuracy of 0.1°C. Uncertainties in the measured and calculated data are estimated based on the method described by Moffat (1988) with a 95% confidence interval. The uncertainty in the Reynolds number is 2.3% at 5000 and below 0.75% for all values of Re above 20,000. Pressure coefficients uncertainties for five-hole probe, static endwall and static pin are below 2.5%. Averaged Nusselt number uncertainties are estimated between 5–10%.

4. RESULTS AND DISCUSSION

The measurements are obtained as the test section reaches a quasisteady state when the pressure and temperature vary by less than 1% over 10 min for Reynolds numbers ranging between 5000 and 50,000. The results are nondimensionalized using the reference properties in Table 1. The air density and viscosity (ρ, μ) in the table are calculated from the pressure and temperature (p_o, T_o) values measured at the inlet of the test section. For comparison, the results are presented as “sidepins” and “no sidepins” for the cases with the sidepins and without the sidepins, respectively. All

TABLE 1: Reference properties used in the results

ρ, kg/m^3	μ, Pa·s	p_o, Pa, abs	T_o, °C	U, m/s
1.00	$1.85 \cdot 10^{-5}$	86,400	25.5	0.8–7.3

the pressure measurements are obtained with adiabatic wall conditions. Also, the flow is considered incompressible because of the small pressure drop across the test section.

4.1 Friction Factors f

The wall-static pressure drop along the streamwise direction is defined in Eq. (1). The local pressure p_x in Eq. (1) is measured at the pressure tap locations along y = 0 on the endwall [see Fig. 1(b)]. The reference pressure p_o is obtained at p_x ($x = 0$, $y = 0$)

$$C_p = \frac{(p_o - p_x)}{0.5\rho U^2}. \tag{1}$$

The effects of the sidepins on the overall pressure penalty in the pin-fin channel as the Re number varies are presented as the friction factor in Fig. 2. The friction factor, f, is estimated from Eq. (2) using the average slopes of the line-fits through C_p versus x/D data by the method described in Pretorius et al. (2017). The quantity $dC_p/d(x/D)$ in the equation is the average slope of C_p versus x/D data for $x/D > 5$, where the flow is fully developed, i.e., the C_p distribution along x/D has a constant slope:

$$f = \frac{dp}{dx}\frac{D_h}{0.5\rho U^2} = \frac{dC_p}{d(x/D)}\frac{D_h}{D}. \tag{2}$$

As indicated in Fig. 2, the f values decrease as the Re number increases with and without the sidepins. However, the f distributions are smaller for the no sidepins case than for the sidepins case as the sidepins introduce higher flow blockage in the channel. The difference in f for the sidepins and no sidepins is reduced as Re increases. At high Re, the mass flow prefers the middle cross section of the channel to the cross section near the sidewall. The blockage through the middle cross section of the channel is the same for both sidepins and no sidepins cases reducing the difference in f in Fig. 2 at higher Re. A correlation in the form of Eq. (3) is developed to predict the experimental data in Fig. 2 separately for the sidepins and no sidepins cases and plotted as a solid line. Table 2 provides the values for the parameters a and b of Eq. (3). The goodness of fit of the present correlations to the experimental data is about 0.98. The f–Re correlation from Metzger et al. (1982) is also given by Eq. (3) with the correlation parameters

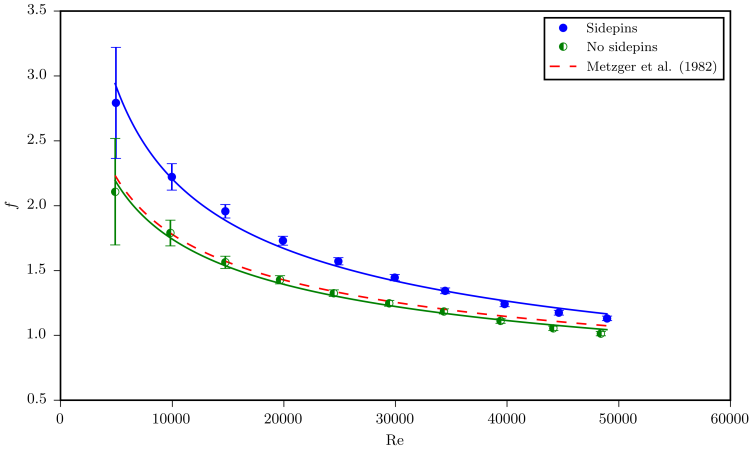

FIG. 2: Friction factor f relative to Re increases with and without sidepins

TABLE 2: Correlation parameters used in Eq. (3) to Eq. (4) for $\mathrm{Re} \leq 50{,}000$

Parameter	Sidepins	No sidepins	Metzger et al. (1982)
a	72.9	30.60	34.61
b	–0.379	–0.315	–0.318
c	2.11	0.884	1
d	–0.0610	0.003	0

being given in Table 2 and plotted as the dashed line in Fig. 2 for comparison. The geometric constraints in the f–Re correlation of Metzger et al. (1982) are adjusted to fit the present definition of friction factor and Re. As clearly shown in Fig. 2, the present correlation and that from Metzger et al. (1982) without the sidepins differ by 6% as the Metzger correlation includes the pressure drop in the developing section of pin-fin array. The correlation from Metzger et al. (1982) underpredicts the experimental data with sidepins by 30% at low Re and by 15% at high Re. A new f–Re correlation in Eq. (4) is developed by adjusting the Metzger et al. (1982) correlation and is expected to predict the friction factor in any pin-fin channel employing the cylindrical pins in the staggered array configuration. The (c, d) parameters of the new correlation in Eq. (4) are provided in Table 2 and f_{metzger} is given by Eq. (3) for Metzger et al. (1982). The maximum difference between Eq. (4) and the sidepin experimental data is then 5%:

$$f = a\mathrm{Re}^{b}, \tag{3}$$

$$f_{o1} = f_{\mathrm{metzger}}[c\mathrm{Re}^{d}]. \tag{4}$$

4.2 Endwall Pressure Coefficients $C_{p,e}$

The static pressure distributions along the endwall are responsible for the local flow field on and near the endwall and affect the local heat transfer distributions on the endwall between the pins. The flow near the endwall region results in the enhanced convective heat transfer in the pin-fin channel. Figure 3 presents the endwall pressure coefficient, $C_{p,e}$, distributions at the endwall location between pin rows 3 and 4. These locations are also identified in Fig. 1(b). The locations of the pins in the measurement area are indicated by the dark quarter-circled regions. Equation (1) with p_x as the local endwall pressure is used to compute $C_{p,e}$ in Fig. 3. The reference pressure p_o in the equation is now obtained at p_x ($x/D = 0$, $y/D = 0$) for each endwall location, where ($x/D = 0$, $y/D = 0$) is the local origin relative to the center of pin row 3. The mean flow is directed along increasing x/D in the figures. The $C_{p,e}$ results in the figures are compared between the cases of sidepins and no sidepins at $\mathrm{Re} = 20{,}000$ and 50,000. The contour levels for both parts of Fig. 3 are shown using one single legend at the bottom of Fig. 3(b). At a given Re and the corresponding locations in Fig. 3, the comparisons show insignificant differences in $C_{p,e}$ distributions between sidepins and no sidepins. In general, the figures show contours of low $C_{p,e} \leq$ –1.4 upstream of a pin in the stagnation region ($1.25 < x/D < 1.5$) because of increased p_x and reverse flow in the the horseshoe vortex (Won et al., 2004). Values of $-1.2 < C_{p,e} < 1.2$ occur downstream of a pin in the wake region ($0.5 < x/D < 0.75$) because of the adverse pressure gradient in the reverse wake flow (Won et al., 2004). High values of $C_{p,e} \geq 1.8$ occur in between two pins of a row ($1.75 < x/D < 2.0$) because p_x decreases to accelerate the flow (Won et al., 2004). As indicated by Won et al. (2004) and Chyu and Goldstein (1991), the endwall heat transfer is expected to be higher in the stagnation horseshoe-vortex region and flow acceleration region between two pins of a given row and lower in the wake region of the pin downstream location. The similarity in the $C_{p,e}$ distributions between sidepins and no sidepins in Fig. 3(a,b) signifies that the local flow field adjacent to the endwall between the pins does not experience the influence when the sidepins are employed at the same Re as for the no sidepins. To show any differences in $C_{p,e}$ contour distributions between the sidepins and no sidepins, local $C_{p,e}$ values along the transverse pitchwise direction y/D at three streamwise positions of $x/D = 0.6$, 1.4, and 2.0 are plotted in Fig. 3(c) for $\mathrm{Re} = 20{,}000$. The data are obtained from the local $C_{p,e}$ distributions between

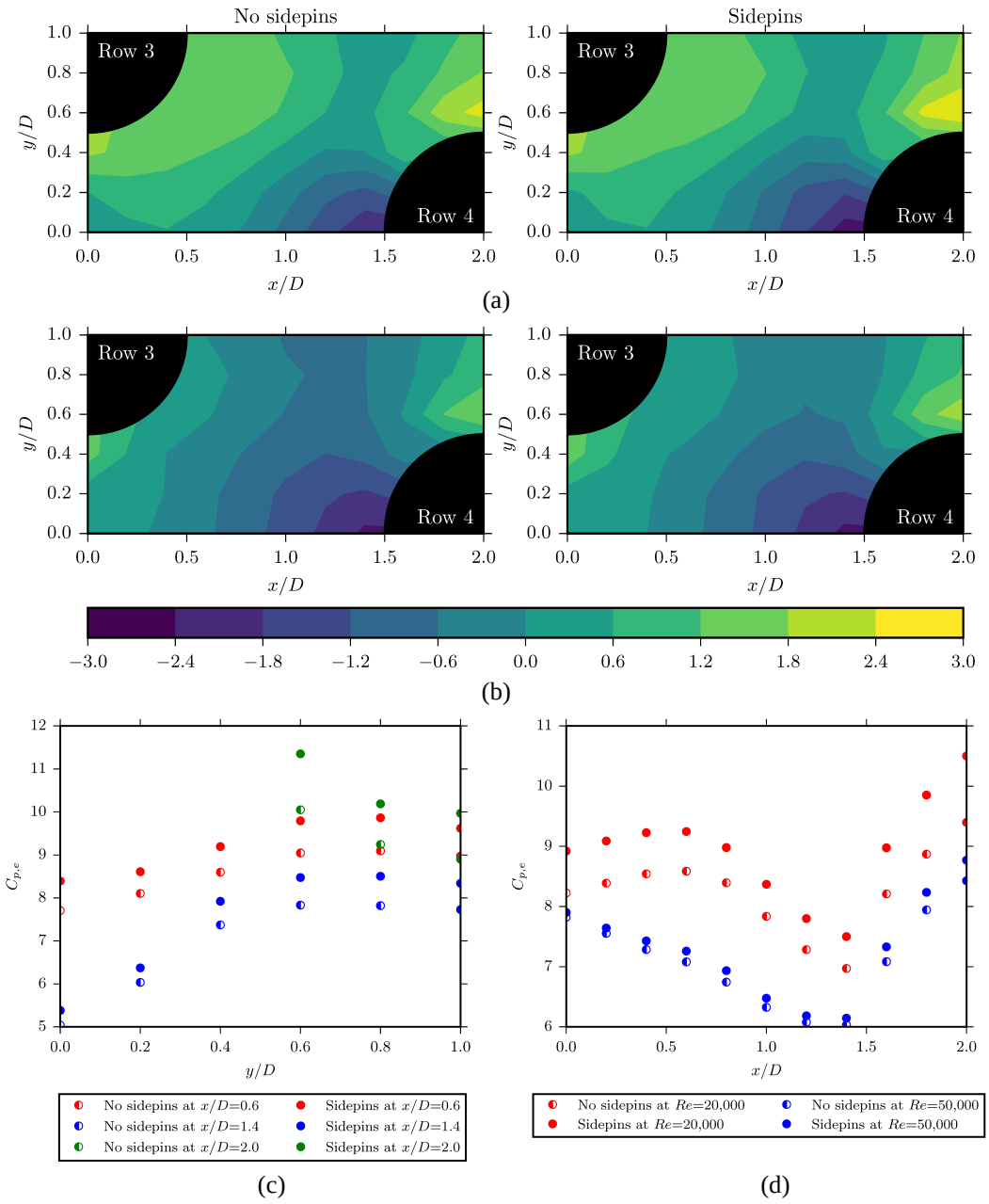

FIG. 3: Endwall pressure coefficients, $C_{p,e}$, between pin rows 3 and 4 with and without sidepins at (a) $\mathrm{Re} = 20{,}000$ and (b) $\mathrm{Re} = 50{,}000$. (c) The transverse pressure coefficient at $\mathrm{Re} = 20{,}000$ for $x/D = 0.6$, 1.4, and 2.0. (d) The average transverse pressure coefficients along the streamwise direction at $\mathrm{Re} = 20{,}000$ and $\mathrm{Re} = 50{,}000$.

pin row 3 and pin row 4. The solid line in the figure represents the sidepins case while the dotted lines represent the no sidepins case. The streamwise locations correspond to the downstream wake region of pin row 3, upstream horseshoe vortex region of pin row 4, and flow acceleration region between pins of row 4, respectively. The $C_{p,e}$ values for the sidepins case in Fig. 3(a) are slightly higher than those for the no sidepins case because the sidepins of row 4 force more flow through the middle cross-section region causing the higher pressure drop ($p_o - p_x$). The mass flux through the sidewall gap is higher for the no sidepins case than for the sidepins case because of no flow

blockages through the sidewall gap. The differences in $C_{p,e}$ of Fig. 3(a) between the cases are reduced as the Re number increases which is evidenced in the average $C_{pe,av}$ distributions along the steamwise x/D for $\mathrm{Re} = 20{,}000$ and 50,000 in Fig. 3(d) for the two cases. The local $C_{p,e}$ values along the transverse y/D at a given x/D position are averaged arithmetically to compute $C_{pe,av}$. The dip in $C_{pe,av}$ near $x/D = 1.4$ of Fig. 3(d) is caused by the smaller values of $(p_o - p_x)$ in the horseshoe-vortex region upstream of pin row 4. In the downstream region of pin row 4, the local flow is fully developed where the $C_{p,e}$ distributions then also show very little differences between the cases of sidepins and no sidepins as expected. The comparisons of $C_{p,e}$ between the two cases downstream of the pin row 4 are thus not presented for brevity.

4.3 Total Pressure-Loss Coefficient $C_{p,t}$

The total pressure loss coefficient $C_{p,t}$ is computed from the measured local total pressure $p_{t,x}$ using Eq. (5) in the transverse normal planes. The reference total pressure $p_{t,o}$ in the equation is measured at $6.5D$ upstream of the 1st pin-row in the smooth inlet of the channel. The $C_{p,t}$ estimates the total pressure penalty and pumping power requirement of flow through the pin rows for a given mass flow rate. The coefficient also indicates the local velocity or mass flow deficit region in the pin rows where the endwall heat transfer can be affected

$$C_{p,t} = \frac{(p_{t,o} - p_{t,x})}{0.5\rho U^2} \tag{5}$$

Figure 4(a,c) present the $C_{p,t}$ distributions in the transverse normal planes $0.9D$ downstream of pin row 3. The data are presented for $\mathrm{Re} = 50{,}000$ and compared between the sidepins and no sidepins case. One single contour legend for all the data is shown at the bottom of Fig. 4. In the figures, the higher the magnitudes of $C_{p,t}$, the higher the total pressure losses and the smaller the local mass flux relative to the other regions in the same plane. The pin location is identified in Fig. 4(a,b) by a pair of vertical dotted lines. Also, $z/H = 0$ and $\pm$ 0.5 refer to the mid-height and endwalls of the channel, respectively. The $C_{p,t}$ data in the middle of the measurement planes in $-0.5 \leq y/D \leq 0.5$ of Fig. 4(a,b) are the highest. In Fig. 4(a), the higher $C_{p,t}$ values are caused by the wake flows (Uzol and Camci, 2005; Won et al., 2004) from pin row 3. In Fig. 4(a), the $C_{p,t}$ distributions are generally higher for the sidepins case than for the no sidepins case because of the additional blockage of the flow cross section by the sidepins in the sidewall gap at row 4.

Figure 4(b,d) presents the nondimensional, velocity-weighted total pressure-loss coefficient $u^* C_{p,t}$ obtained by simply multiplying the local u^* with $C_{p,t}$. The ratio u/U in the definition of u^* also implies the local mass flux ratio in the incompressible flow of the pin-fin test section. The $u^* C_{p,t}$ data distributions are shown in the same planes as those in Fig. 4(a) at $\mathrm{Re} = 50{,}000$ and indicate the direct influences of the local mass flux redistributions when the sidepins are employed. The distributions in Fig. 4(b) are higher for the sidepins case than for the no sidepins case as the local mass-flux, or u^*, is higher downstream of the pin row with sidepins. However, $u^* C_{p,t}$ valuers directly downstream of the pin region in $-0.5 < y/D < 0.5$ are substantially lower than in other regions either for sidepins or no sidepins because of low mass flux downstream of the pin and high mass flux in-between the pins of row 4. The data in the plots of Figs. 4(c,d) simply illustrate the comparison of $C_{p,t}$ and $u^* C_{p,t}$ further between sidepins and no sidepins at two heights of the channel ($z/H = 0$, 0.47) at $0.9D$ downstream of pin row 3. The Reynolds number for the data is also 50,000, the same as that for Fig. 4(a,b). The differences of the data in Fig. 4 between sidepins and no sidepins become smaller as Re decreases and are evidenced in the average total pressure loss $C_{pt,av}$ presented in Fig. 5(a).

The local $C_{p,t}$ data in the same transverse plane as in Fig. 4(a) are mass-averaged to present the globally averaged loss coefficient $C_{pt,av}$ in Fig. 5(a) at different Re. The mass average is computed based on the mass averaging equation of local losses in Mahmood and Arnachellan (2018). The average $C_{pt,av}$ magnitudes with or without sidepins in Fig. 5(a) decrease as the Re number increases. However, the sidepins $C_{pt,av}$ is always higher than the no sidepins $C_{pt,av}$ and the difference between the two cases seems to increase at higher Re. The redistribution effects of the local mass flux and accelerations of flow, that are responsible for higher local mass flux and $u^* C_{p,t}$ values, are higher and more dominant as Re increases for the sidepins case. Figure 5(a) shows the global mass-averaged loss coefficient, $C_{pt,av}$ versus Re in the transverse normal plane $0.9D$ downstream of pin row 11. The $C_{pt,av}$ value of Fig. 5(b) is computed

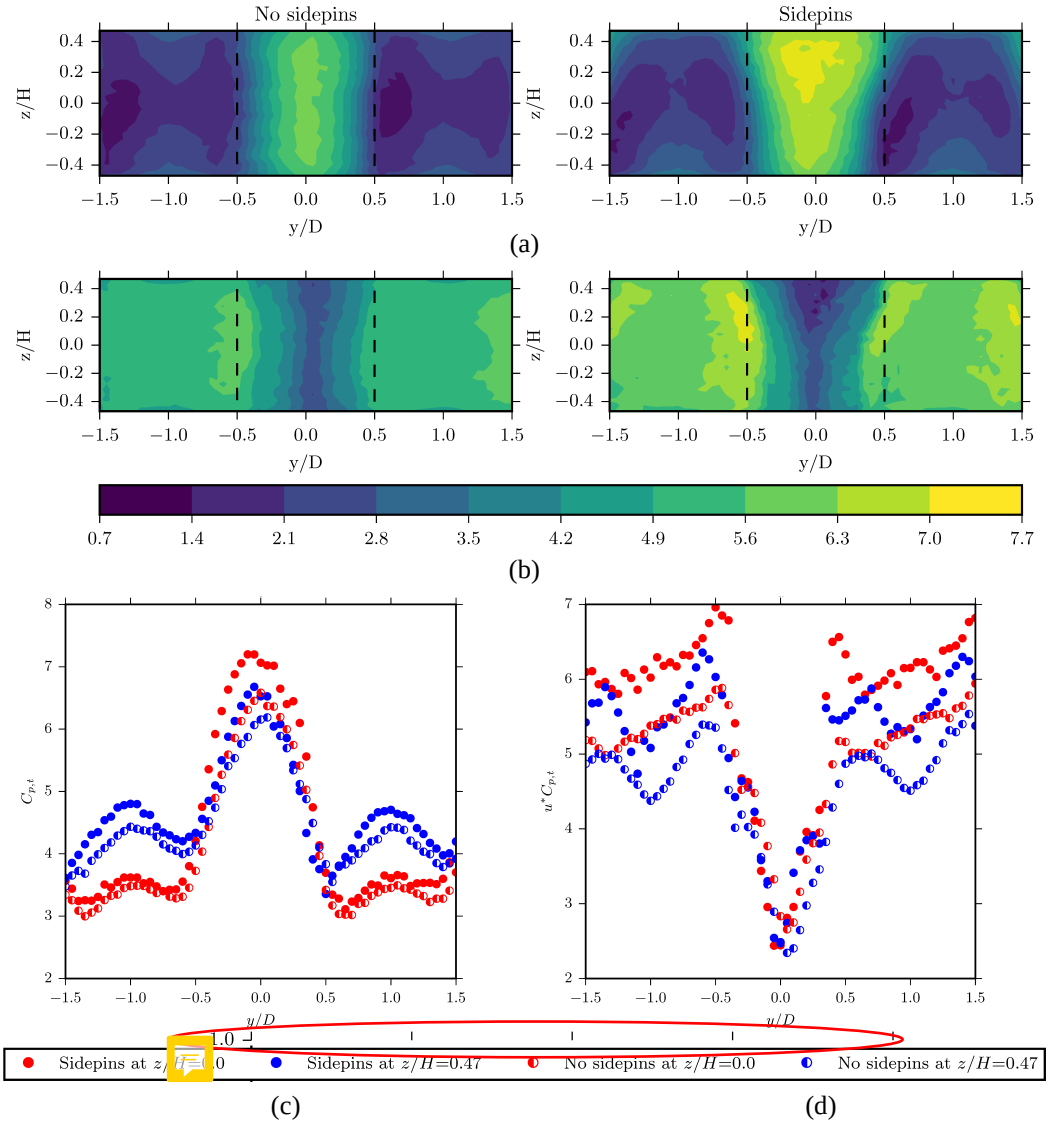

FIG. 4: (a) Total pressure-loss coefficients, $C_{p,t}$ and (b) velocity-weighted total pressure-loss coefficients, $u^*C_{p,t}$ in the transverse plane $0.9D$ downstream of row 3 with and without sidepins at $\mathrm{Re} = 50{,}000$. (c) Total pressure-loss coefficients, $C_{p,t}$ and (d) velocity-weighted total pressure-loss coefficients, $u^*C_{p,t}$ distributions at $z/H = 0.0$ and $z/H = 0.47$ at $\mathrm{Re} = 50{,}000$.

from the local $C_{p,t}$ and u^* distributions in the plane. Note, the $C_{pt,av}$ value in Fig. 5(b) also decreases as the Re number increases and is higher for the sidepins than for the no sidepins; however, the difference of $C_{pt,av}$ between the sidepins and no sidepins in the plane of Fig. 5(b) decreases as the Re number increases. The effects of higher mass flux with the sidepins than without the sidepins in row 12 thus gradually dimimish as the Re number increases. The pumping power requirements then in the pin-fin channel of 11 or more pin rows with and without the sidepins might not be significantly different from one an other when $\mathrm{Re} > 50{,}000$.

4.4 Endwall Nusselt Numbers

Endwall Nusselt number values between pin rows 3 and 4 in the rectangular region on endwall of Fig. 1(b) are estimated based on Eqs. (6) and (7). The Nusselt numbers are then normalized by the smooth channel Nu_0 measured

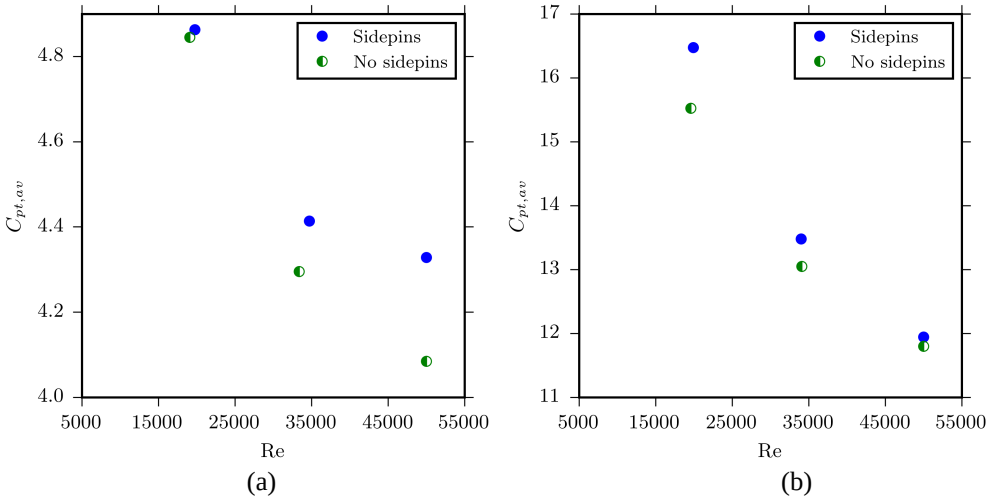

FIG. 5: Mass-averaged total pressure coefficents $C_{pt,av}$ downstream of (a) pin row 3 and (b) pin row 11

in the pin-fin test section without pin fins. The Nu_0 values are obtained at the thermally developed section in the smooth channel at the same Re as in the pin-fin channel. The normalized data, $\mathrm{Nu}^* = \mathrm{Nu}/\mathrm{Nu}_0$ for $\mathrm{Re} = 20{,}00$ and $\mathrm{Re} = 50{,}000$, are then presented in Fig. 6(a,b), respectively, and compared between the sidepins and no sidepins cases. The average heat flux level, $Q_c/(A_s)$, is different for the sidepins and no sidepins cases in Fig. 6 to maintain a temperature difference $(T_{w,x} - T_{m,x})$ of about 40°C in Eq. (7). However, measurements obtained at different flux levels at a Re [Q1] indicate insignificant dependence of Nu on heat flux for both cases. The quantity $\Sigma Q_{c,x}$ in Eq. (6) is the total convective power from the start of pin row to a distance x at two endwalls. The heater area covered under the pin base is accounted in $\Sigma Q_{c,x}$ of Eq. (6) as the heat from the pin base contributes to the flow heating. The air properties (c_p, k_a) are taken at T_o as the temperature difference between the inlet and exit air of test section does not exceed 15°C:

$$T_{m,x} = T_0 + \frac{\Sigma Q_{c,x}}{M_a c_p}, \tag{6}$$

$$\mathrm{Nu} = \frac{Q_c D_h}{A_s (T_{w,x} - T_{m,x}) k_a}. \tag{7}$$

The Nu^* distributions on the bottom endwall in Fig. 6(a,b) are presented with the constant value of Nu_0 at $\mathrm{Re} =$ 20,000 and 50,000 and thus, indicate the Nu distributions primarily influenced by the local secondary flows between the pin rows. The locations of the pin bases in rows 3 and 4 are indicated in Fig. 6(a,b) by the dark quarter-circled regions. The contour values in the color distributions are provided in a single legend at the bottom of Fig. 6(b). The Nu^* distributions increase along downstream of the pin in row 3 and as the stagnation region of the pin in row 4 is approached because of the wake flows and leading-edge horseshoe vortex (Won et al., 2004), respectively. When compared, the Nu^* values are slightly higher for the sidepins than for the no sidepins case in the region of $x/D \geq$ 1.0 at both Reynolds numbers. The higher mass flux and flow acceleration through the flow cross sections of row 4 with the sidepins increase the local Nu^* value more in $x/D \geq 1.0$ than those for the no sidepins case. The higher mass flux between the pins in row 4 with the sidepins reduces the thermal boundary layer. The structures of the wake region and horseshoe vortex thus seem to slightly influence the change in the local Nu^* number when the sidepins are employed. The streamwise vorticities responsible for the local mixing of fluids between the endwall region and bulk flow show little differences between the sidepins and no sidepins case, and thus, are not presented for brevity. The probe dimensions do not allow one to obtain the secondary flow measurements very close to the endwall to further explain the comparisons in Fig. 6(a,b) between the sidepins and no sidepins. The line plots of Fig. 4(c) further illustrate the local differences of Nu^* between sidepins and no sidepins case at Re = 20,000. The endwall location for the data is between pin rows 3 and 4. The Nu^* values along the transverse y/D are slightly higher at all three

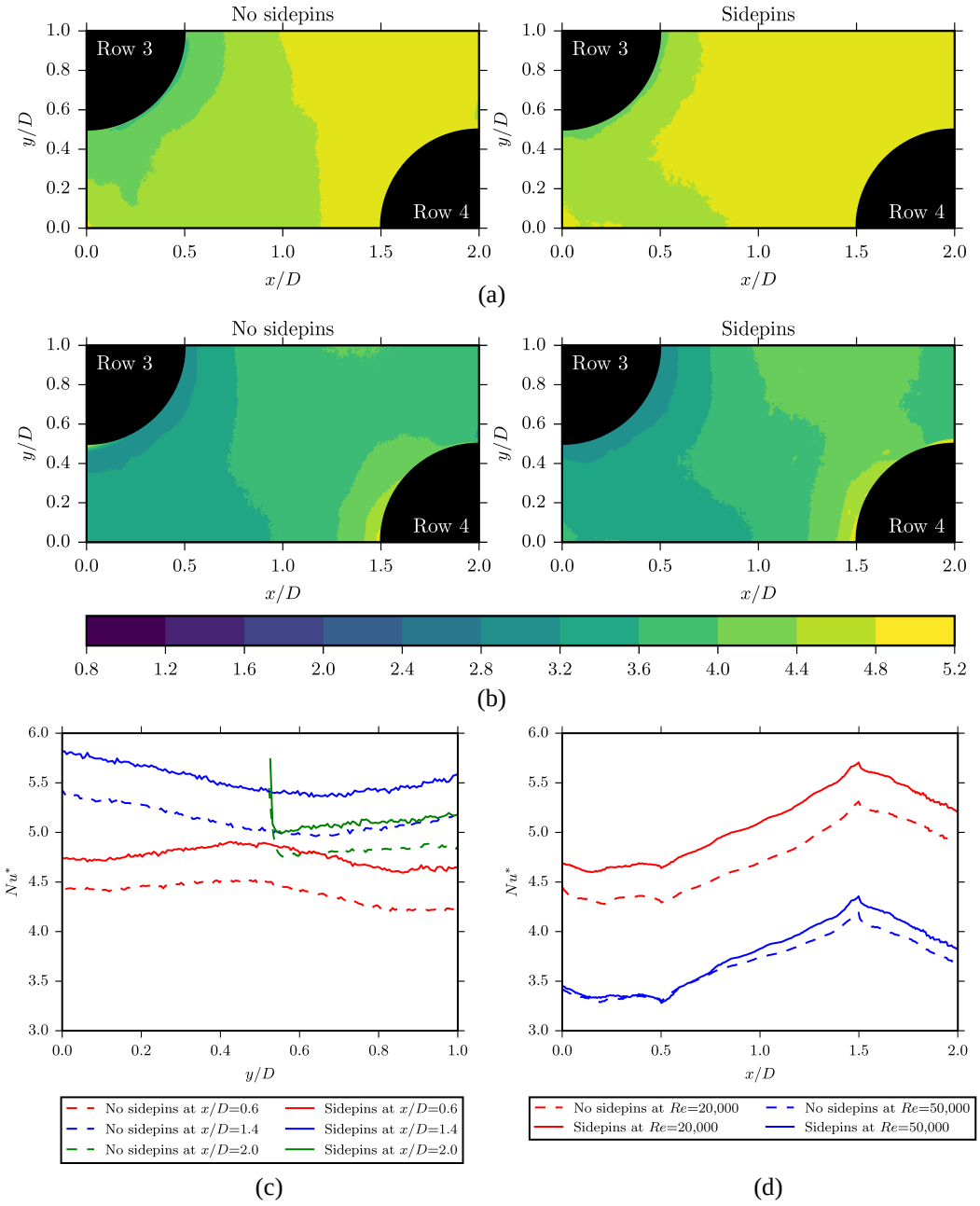

FIG. 6: Normalized endwall Nusselt number Nu^* distributions between pin rows of 3 and 4 with and without sidepins at (a) $\mathrm{Re} = 20{,}000$ and (b) $\mathrm{Re} = 50{,}000$. (c) The transverse endwall Nusselt number, Nu^*, at $\mathrm{Re} = 20{,}000$ for $x/D = 0.6$, 1.4, and 2.0. (d) The average transverse endwall Nusselt number, Nu^*, along the streamwise direction at $\mathrm{Re} = 20{,}000$ and $\mathrm{Re} = 50{,}000$.

streamwise x/D positions in Fig. 4(c) for the sidepins case as expected. The local Nu^* values along y/D are then arithmetically averaged and plotted as Nu^*_{av} versus x/D in the region between pin rows 3 and 4 in Fig. 4(d) for $\mathrm{Re} = 20{,}000$ and 50,000. The Nu^*_{av} values are slightly higher (about 4% to 9%) for the sidepins than for the no sidepins case when $\mathrm{Re} = 20{,}000$. The difference in Nu^*_{av} are then much smaller between the two cases when $\mathrm{Re} = 50{,}000$ in Fig. 4(d).

Figure 7(a,b) presents the area-averaged Nusselt numbers Nu_{av} between pin rows 3 and 4 and between pin rows 11 and 12 for different Re, respectively. The uncertainty bars on the data are indicated. The average is computed based on the pixel dimensions in the infrared images and local Nu data such as those in Fig. 6(a,b). The Nu_{av} number in Fig. 7(a,b) increases with Re and mass flow rate as expected with and without the sidepins. In Fig. 7(a), the Nu_{av} values in the region between pin rows 3 and 4 are slightly higher for sidepins than for no sidepins at lower Re and are then about the same for the two cases at higher Re. The difference in Nu_{av} between the sidepins and no sidepins case at a Re [Q2] in Fig. 7(b) is marginal and falls within the uncertainty limits. The solid lines in Fig. 7(b) are plotted using the correlation of Eq. (8) developed from the present experimental data in the region between pin rows 11 and 12 where the flow is fully developed thermally and hydraulically. The correlation has the same form as that of Metzger et al. (1982). Table 3 provides the coefficients (a, b) in Eq. (8) for all the cases including those in Metzger et al. (1982). The present correlation [Eq. (8)] falls well within the uncertainties of the experimental data and differs by maximum 7% from the experimental data. The dotted line in Fig. 7(a) represents the Metzger et al. (1982) correlation in a pin-fin channel. While the Metzger et al. (1982) correlation is developed using the data in both thermally developing and developed regions, the present correlation in Eq. (8) uses only the data in the thermally developed region. The Nu_{av} data are normalized by the smooth channel Nu_0 at the corresponding Re and plotted as Nu^*_{av} in Fig. 7(a,b) as Re varies. The Nu^*_{av} values in Fig. 7(a,b) decrease as the Re number increases, but are slightly higher for sidepins than

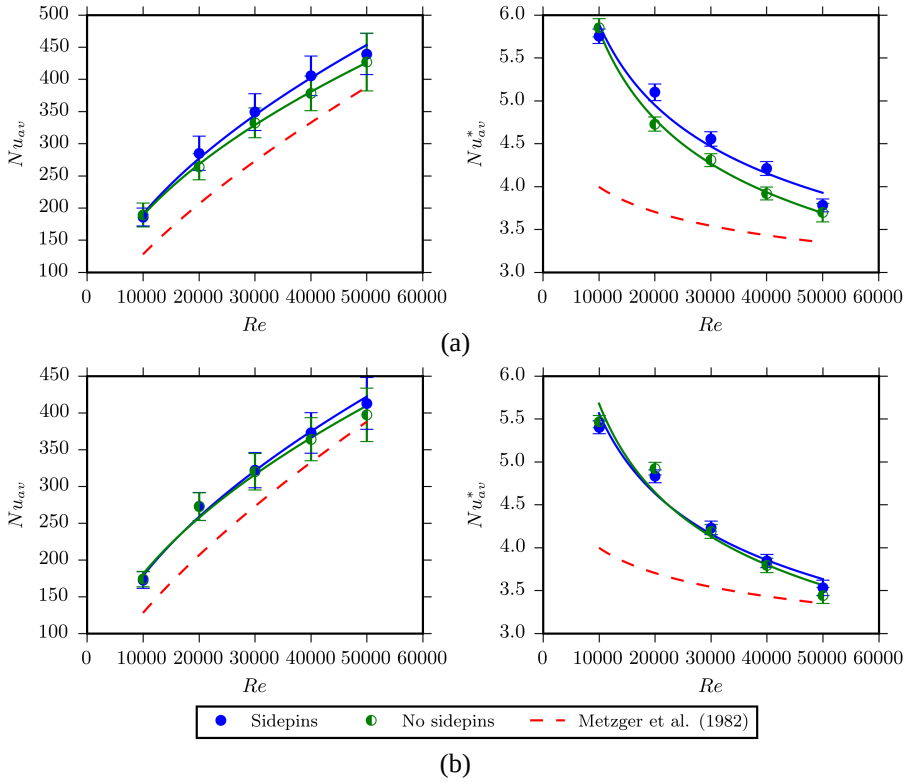

FIG. 7: Area-averaged $\mathrm{Nu}_{\mathrm{avg}}$ and $\mathrm{Nu}^*_{\mathrm{avg}}$ between (a) pin rows 3 and 4 and (b) pin rows 11 and 12 with and without sidepins as Re varies

TABLE 3: Correlation parameters used in Eq. (8) for $\mathrm{Re} \leq 50{,}000$

Parameter in Eq. (8)	Sidepins	No sidepins	Metzger et al. (1982)
a	1.14	0.573	0.222
b	0.536	0.604	0.690

for no sidepins in Fig. 7(a) at lower Re values. As shown, the Nu^*_{av} values in Fig. 7(b) differ little in the cases with and without the sidepins. The normalized correlations obtained by dividing Eq. (8) by Nu_0 are also shown in Fig. 7(b) as the solid and dotted lines

$$\mathrm{Nu}_{av} = a\mathrm{Re}^b. \tag{8}$$

4.5 Flow Temperature

Air temperature distributions indicate the results of turbulent mixing between the local hot and cold fluids in the pin rows. In the present measurements, the hot fluid is present near the endwalls and pin surface. The core flow in the channel contains the cold fluid. The mixing of fluids, heat transfer coefficients, and cooling of the walls are usually high when the temperature profile in the flow cross section is uniform. The uniform temperature profile is also important for the air flow exiting the heat exchanger and combustor cooling liner. The exiting flow from the channel is then used for space heating/cooling or fuel combustion. The uniform temperature profile of the fully developed flow in the flow cross section downstream of pin rows is thus desirable. The nondimensional air temperature, T^*, contours at $\mathrm{Re} = 50{,}000$ are shown in Fig. 8 in the transverse plane downstream of row 11 and are compared between the sidepins and no sidepins cases. The flow is thermally developed at this measurement plane. The velocity-weighted T^* determined from the measured T values in Eq. (9) also indicates the mass-flux weighted local temperature for the incompressible flow. The local mixed-mean $T_{m,x}$ is obtained from Eq. (6) at the streamwise location of the measurement plane and is a constant in Eq. (9) for the data in Fig. 8. However, $T_{m,x}$ for the no sidepins is different from the sidepins so as to maintain $(T_{w,x} - T_{m,x}) \approx 40$°C. The data in Fig. 8 are presented for the spacing of $y = 2D$ and from the endwall to mid-channel height ($0 \geq z \geq -0.5H$) because of the symmetry. The pin location in the 11$^{\text{th}}$ row is indicated between the dotted lines. The region between the dotted lines contains the wake flows from the pins of row 11 as well as starts to experience the flow acceleration due to the approach of reduced cross section between the two pins of row 12. Note that unlike the distributions in Fig. 8, for air heating in a smooth channel the temperatures in a flow cross section would have decreased from the endwall toward the mid-height with uniform temperatures along y/D. The high values of T^* from Eq. (9) generally refer to the hotter air temperatures T and $T_{m,x}$

$$T^* = \frac{u^* T}{T_{m,x}}. \tag{9}$$

The significant variations of T^* in Fig. 8 with or without the sidepins occur along transverse pitch in –0.5 $< y/D <$ 0.5 in the wake region directly downstream of the pin. The high values of u^* due to the flow acceleration and high mass flux bring the colder fluid from the channel core and cause low values of T^* in the pin wake region. Note, the plane location of Fig. 8 corresponds to $x/D = 1.4$ in Fig. 6. The endwall Nusselt numbers at this downstream location of the pin row, i.e., between –0.5 $< y/D <$ 0.5 are generally high. The almost uniform distribution of T^* outside the wake region ($y/D >$ 0.5 and $y/D <$ –0.5) in Fig. 8 indicates the strong influences of three-dimensional vortical motions advected from the pin-leading edge in mixing the fluids. The differences in the T^* distributions

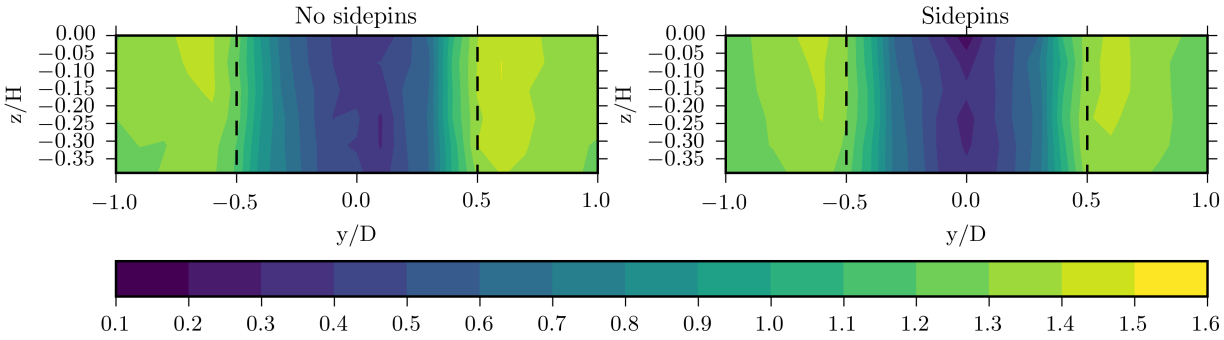

FIG. 8: Nondimensional velocity weighted air temperature, T^* in the transverse plane $0.9D$ downstream of pin row 11 at $\mathrm{Re} =$ 50,000 with and without sidepins

between the sidepins and no sidepins are marginal. At $\mathrm{Re} < 50{,}000$, the distributions and comparisons of T^* between the sidepins and no sidepins are about the same as those in Fig. 8 and are not presented for brevity.

5. CONCLUSIONS

Measurements of the pressure distributions, pressure drops, friction factors (f), flow temperature, and endwall Nusselt numbers (Nu) along a pin-fin channel of aspect ratio 7.81:1 are presented with and without the presence of pins on the channel sidewall. Circular pins are employed in staggered rows in equal pitch in both streamwise and transverse directions. The Reynolds number (Re) in the channel based on the mean flow velocity varies between 5000 and 50,000. The sidepins are employed in the even numbered pin rows so that the number of pins in each streamwise pin row is the same. When the sidepins on the walls are employed, the flow cross section and blockage ratio in each pin row also become the same. The objectives are to estimate the effects of sidepins on the measured results in a rectangular channel of small aspect ratio. The measurements are obtained in the flow developing region upstream of pin row 4 as well as in flow developed region downstream of pin row 11. The results in the developing region are important because of the applications of short-length cooling channels with few rows of pin fins in constrained spaces. The investigated channel thus simulates the cooling and heat transfer channels in electronic components, machines housings, bearing and braking pads, fuel cells, gas turbine blades, etc. The summary results and conclusions on the results are as follows:

1. Secondary flow field and flow developing region along the channel are not influenced when the sidepins are employed. However, the local mass flux and accelerations of flow increase in the flow cross sections between the pins in the rows where the sidepins are present.

2. The friction factor in the channel increases with sidepins as they provide additional flow blockage in the channel for any Reynolds number tested. The friction factor in general decreases as the Reynolds number increases with or without the sidepins. However, the friction factor is 30% higher at $\mathrm{Re} = 5000$ and 15% higher at $\mathrm{Re} = 50{,}000$ for the case with sidepins than for the no sidepins case as the differences in friction factors between the two cases decrease as the Reynolds number increases.

3. Simple correlations between the friction factor and Reynolds number (f–Re) are developed with reasonable accuracy to predict the present experimental results with and without the sidepins. A simple correction to the f–Re correlation by Metzger et al. (1982) is offered that can predict the friction factor in the present circular pin-fin channel with the sidepins.

4. Endwall static-pressure distributions between the pin rows are marginally affected as the sidepins are employed indicating the local flow structures adjacent to the endwall are also not influenced.

5. The total pressure-loss distributions in the flow cross sections downstream of a pin-row change and consequently, the average total loss coefficients become higher when the sidepins are employed because of the additional flow blockages and redistributions of the mass flux and accelerations of local flow. However, the differences in the global mass-averaged total pressure loss coefficients between the cases of sidepins and no sidepins decrease as the Reynolds number increases. The average total pressure loss is 6% higher at Re = 10,000 and only 1% higher at $\mathrm{Re} = 50{,}000$ with the sidepins. The pumping power requirements are thus not much different with and without the sidepins at $\mathrm{Re} \geq 50{,}000$. In the flow developing region on the contrary, the mass-averaged loss coefficients for the sidepins differ significantly from those for the no sidepins case at higher Reynolds numbers. The pumping power requirements at high Reynolds numbers, i.e., $\mathrm{Re} > 30{,}000$ then become much higher for the sidepins case than for the no sidepins case which are undesirable for the short-length pin-fin channels in electronic components.

6. The average Nusselt numbers and ratios of average Nusselt number to smooth channel Nusselt number on the endwall in both developing and developed flow regions are marginally higher for the sidepins case than for the no sidepins case as the local mass flux and acceleration are higher with the sidepins. The average differences

are higher for the sidepins than for the no sidepins case at the low Reynolds numbers in the flow developing region. The local temperature field downstream of the pin row 11, where the flow is fully developed, is almost the same for the sidepins and no sidepins cases to suggest the secondary flows responsible for the flow mixing are indifferent when the sidepins are employed.

As the estimates of pumping power and local heat transfer coefficients are very important in the applications of the pin-fin channel, the present investigation will contribute to the design and predictions of thermal performance of the circular pin-fin channels.

ACKNOWLEDGMENTS

The work was financially supported by the NRF of South Africa and ARMSCOR of the South African Department of Defence.

REFERENCES

Ames, F., Dvorak, L., and Morrow, M., Turbulent Augmentation of Internal Convection over Pins in Staggered Pin Fin Arrays, *J. Turbomach.*, vol. **127**, pp. 183–190, 2005.

Armstrong, J. and Winstanley, D., A Review of Staggered Array Pin Fin Heat Transfer for Turbine Cooling Applications, *J. Turbomach.*, vol. **110**, pp. 94–103, 1988.

Axtmann, M., Poser, R., von Wolfersdorf, J., and Bouchez, M., Endwall Heat Transfer and Pressure Loss Measurements in Staggered Arrays of Adiabatic Pin Fins, *Appl. Therm. Eng.*, vol. **103**, pp. 1048–1056, 2016.

Chang, S., Yang, T., Huang, C., and Chiang, K., Endwall Heat Transfer and Pressure Drop in Rectangular Channels with Attached and Detached Circular Pin-Fin Array, *Int. J. Heat Mass Transf.*, vol. **51**, pp. 5247–5250, 2008.

Chyu, M. and Goldstein, R., Influence of an Array of Wall-Mounted Cylinders on the Mass Transfer from a Flat Surface, *Int. J. Heat Mass Transf.*, vol. **34**, pp. 2175–2186, 1991.

Chyu, M., Hsing, Y., and Natarajan, V., Convective Heat Transfer of Cubic Fin Arrays in a Narrow Channel, *Trans. ASME*, vol. **120**, pp. 362–367, 1998.

Goldstein, R., Jabbari, M., and Chen, S., Convective Mass Transfer and Pressure Loss Characteristics of Staggered Short Pin-Fin Arrays, *Int. J. Heat Mass Transf.*, vol. **37**, pp. 149–160, 1994.

Huang, S., Maltson, J., and Yan, Y., Experimental Study on Heat Transfer Improvement Structures with Staggered Transverse Elongated Pedestal Array, *Int. J. Heat Mass Transf.*, vol. **97**, pp. 502–510, 2016.

Lawson, S., Thrift, A., Thole, K., and Kohli, A., Heat Transfer from Multiple Row Arrays of Low Aspect Ratio Pin Fins, *Int. J. Heat Mass Transf.*, vol. **54**, pp. 4099–4109, 2011.

Li, Q., Chen, Z., Flechtner, U., and Warnecke, H.J., Heat Transfer and Pressure Drop Characteristics in Rectangular Channels with Elliptic Pin Fins, *Int. J. Heat Mass Transf.*, vol. **19**, pp. 245–250, 1998.

Ligrani, P., Singer, B., and Baun, L., Miniature Five-Hole Pressure Probe for Measurement of Three Mean Velocity Components in Low-Speed Flows, *J. Phys. E: Sci. Instrum.*, vol. **22**, pp. 868–876, 1989a.

Ligrani, P., Singer, B., and Baun, L., Spatial Resolution and Downwash Velocity Corrections for Multiple-Hole Pressure Probes in Complex Flows, *Exp. Fluids 7*, vol. **6**, pp. 424–426, 1989b.

Mahmood, G. and Arnachellan, K., Effects of Upstream Endwall Film Cooling on a Vane Cascade Flowfield, *J. Propuls. Power*, vol. **34**, no. 2, pp. 460–468, 2018.

Metzger, D., Fan, Z., and Shepard, W., Pressure Loss and Heat Transfer through Multiple Rows of Short Pin Fins, *Proc. Seventh Int. Heat Transf. Conf.*, vol. **3**, pp. 137–142, 1982.

Moffat, R., Describing the Uncertainties in Experimental Results, *Exp. Therm. Fluid Sci.*, vol. **1**, pp. 3–17, 1988.

Paul, R., Upadhyay, R., and Jain, A., A Novel Calibration Algorithm for Five-Hole Pressure Probe, *Int. J. Eng. Sci. Technol.*, vol. **3**, no. 2, pp. 89–95, 2011.

Pretorius, H., Mahmood, G., and Meyer, J., Static Pressure Characteristics in a Pin-Fin Channel with Shaped Cylindrical Pins, *J. Fluids Eng.*, vol. **139**, no. 9, p. 091104, 2017.

Rao, Y., Wan, C., and Zang, S., An Experimental and Numerical Study of Flow and Heat Transfer in Channels with Pin Fin–Dimple Combined Arrays of Different Configurations, *J. Heat Transf.*, vol. **134**, no. 12, p. 121901, 2012.

Sargant, S., Hedlund, C., and Ligrani, P., An Infrared Thermography Imaging System for Convective Heat Transfer Measurements in Complex Flows, *Meas. Sci. Technol.*, vol. **9**, pp. 1974–1981, 1998.

Tanda, G., Heat Transfer and Pressure Drop in a Rectangular Channel with Diamond-Shaped Elements, *Int. J. Heat Mass Transf.*, vol. **44**, pp. 3529–3541, 2001.

Uzol, O. and Camci, C., Heat Transfer, Pressure Loss and Flow Field Measurements Downstream of Staggered Two-Row Circular and Elliptical Pin Fin Arrays, *J. Heat Transf.*, vol. **127**, pp. 458–471, 2005.

Won, S., Mahmood, G., and Ligrani, P., Spatially-Resolved Heat Transfer and Flow Structure in a Rectangular Channel with Pin Fins, *Int. J. Heat Mass Transf.*, vol. **47**, pp. 1731–1743, 2004.

Xu, F. and Wu, H., Experimental Study of Water Flow and Heat Transfer in Silicon Micro-Pin-Fin Heat Sinks, *Int. J. Heat Transf.*, vol. **140**, no. 12, p. 122401, 2018.